Acta Pharmaceutica Sinica B 2022;12(6):2695–2709

Chinese Pharmaceutical Association
Institute of Materia Medica, Chinese Academy of Medical Sciences

Acta Pharmaceutica Sinica B

www.elsevier.com/locate/apsb
www.sciencedirect.com

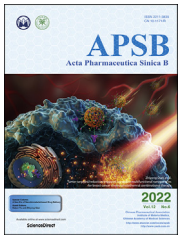

ORIGINAL ARTICLE

Bispecific prodrug nanoparticles circumventing multiple immune resistance mechanisms for promoting cancer immunotherapy

Jiayi Ye[a,b,†], Bo Hou[a,c,†], Fangmin Chen[a,b], Shunan Zhang[a,c], Muya Xiong[b,d], Tianliang Li[a], Yechun Xu[b,d,e], Zhiai Xu[c], Haijun Yu[a,b,*]

[a]*State Key Laboratory of Drug Research & Center of Pharmaceutics, Shanghai Institute of Materia Medica, Chinese Academy of Sciences, Shanghai 201203, China*
[b]*University of Chinese Academy of Sciences, Beijing 100049, China*
[c]*School of Chemistry and Molecular Engineering, East China Normal University, Shanghai 200241, China*
[d]*CAS Key Laboratory of Receptor Research, and Drug Discovery and Design Center, Shanghai Institute of Materia Medica, Chinese Academy of Sciences, Shanghai 201210, China*
[e]*School of Pharmaceutical Science and Technology, Hangzhou Institute for Advanced Study, University of Chinese Academy of Sciences, Hangzhou 310013, China*

Received 5 August 2021; received in revised form 30 August 2021; accepted 7 September 2021

KEY WORDS

Immunotherapy;
Prodrug nanoparticles;
Immune evasion;
Immunogenic cell death;
Tumor microenvironment

Abstract Cancer immunotherapy is impaired by the intrinsic and adaptive immune resistance. Herein, a bispecific prodrug nanoparticle was engineered for circumventing immune evasion of the tumor cells by targeting multiple immune resistance mechanisms. A disulfide bond-linked bispecific prodrug of NLG919 and JQ1 (namely NJ) was synthesized and self-assembled into a prodrug nanoparticle, which was subsequently coated with a photosensitizer-modified and tumor acidity-activatable diblock copolymer PHP for tumor-specific delivery of NJ. Upon tumor accumulation *via* passive tumor targeting, the polymeric shell was detached for facilitating intracellular uptake of the bispecific prodrug. NJ was then activated inside the tumor cells for releasing JQ1 and NLG919 *via* glutathione-mediated cleavage of the disulfide bond. JQ1 is a bromodomain-containing protein 4 inhibitor for abolishing interferon gamma-triggered expression of programmed death ligand 1. In contrast, NLG919 suppresses indoleamine-2,3-dioxygenase 1-mediated tryptophan consumption in the tumor microenvironment, which thus restores robust antitumor immune responses. Photodynamic therapy (PDT) was performed to elicit

*Corresponding author. Tel./fax: +86 21 50802322.
E-mail address: hjyu@simm.ac.cn (Haijun Yu).
†These authors made equal contributions to this work.
Peer review under responsibility of Chinese Pharmaceutical Association and Institute of Materia Medica, Chinese Academy of Medical Sciences.

https://doi.org/10.1016/j.apsb.2021.09.021

antitumor immunogenicity by triggering immunogenic cell death of the tumor cells. The combination of PDT and the bispecific prodrug nanoparticle might represent a novel strategy for blockading multiple immune evasion pathways and improving cancer immunotherapy.

1. Introduction

Immunotherapy, in particular immune checkpoint blockade (ICB) therapy has revolutionized cancer management in clinic. However, current immunotherapy suffers from the low response rate due to occurrence of the intrinsic and adaptive immune resistance[1,2]. Many types of the solid tumors display intrinsic immune evasion due to low immunogenicity of the tumor cells and insufficient intratumoral infiltration of the cytotoxic T lymphocytes (CTLs) for tumor regression[3]. On the other hand, the tumor-infiltrating CTLs can secret proinflammatory cytokine interferon gamma (IFN-γ) for inducing the adaptive immune resistance by activating a series of immunosuppressive factors. For instance, IFN-γ has been identified to upregulate the indoleamine-2,3-dioxygenase 1 (IDO-1) and programed death ligand 1 (PD-L1) through the janus kinase/signal transducer and activator of transcriptions (JAK-STAT) signaling pathway. IDO-1 can metabolize tryptophan (Trp) into L-kynurenine (Kyn) for activation of the regulatory T lymphocytes (Tregs) and depletion of the tumor-infiltrating CTLs[4−8]. In contrast, PD-L1 on the surface of the tumor cell membrane can trigger CTLs exhaustion by ligation of programmed death receptor 1 (PD-1) expressed on the surface of the T cells[9,10]. On top of that, the multiplicity of immune resistance mechanisms and the complexity of cancer-type-dependent immune evasion pathways severely limit the response rate of monotherapy and usually develop immune tolerance to monotherapy[11,12]. Thus, there is a tremendous need for improving current immunotherapy by targeting the multiple immune evasion pathways.

In past years, the combination of two monoclonal antibodies or bispecific antibodies (BiAbs) have been extensively exploited in clinic trails by blocking two immune targets[13−15]. In particularly, the BiAbs have displayed effective antitumor performance due to their advantage for simultaneously blocking two immune targets[16,17]. Despite promising, the BiAbs display several drawbacks, such as on-target but off-tumor effect as the same with monoclonal antibodies, high development costs, poor tumor penetration ability, and incompetence of blocking the intracellular targets. Therefore, a cost-efficient and tumor-specific drug delivery approach for blocking the intracellular targets and improving cancer immunotherapy remains to be optimized.

Recent studies including ours have demonstrated promising potential of the prodrug strategies for co-delivering multiple immunotherapy[18−25]. Up to date, large number of disulfide bond-linked prodrug dimers have been prepared and studied due to the redox-sensitivity and self-assembly[26−28]. To simultaneously address both the innate and adaptive immune resistance in the solid tumors, we herein engineered a bispecific prodrug nanoparticle (NP) by self-assembly of a disulfide bond-linked bispecific prodrug of NLG919 and JQ1, namely NLG919-SS-JQ1 (NJ), which were subsequently coated with a tumor extracellular acidity (*i.e.*, pH $<$ 6.8)-activatable amphiphilic diblock copolymer PHP for tumor-specific delivery of the bispecific prodrugs. PHP was covalently modified with a photosensitizer pyropheophorbide-a (PPa) for photodynamic therapy (PDT) of cancer. Upon tumor accumulation through passive tumor targeting, the polymeric shell PHP could be detached from the prodrug NPs (PHPNJ) for facilitating intracellular uptake of the bispecific prodrug NJ, which could be activated inside the tumor cells *via* glutathione (GSH)-mediated cleavage of the disulfide bond (Fig. 1A). Under the guidance of PPa-mediated fluorescence imaging, PDT can be performed with 671 nm laser for inducing reactive oxygen species (ROS) generation and triggering immunogenic cell death (ICD) of the tumor cells, which promotes dendritic cells (DCs) maturation and elicits antitumor immunogenicity[29]. Furthermore, NLG919 can inactivate IDO-1 for suppressing Trp consumption in the tumor microenvironment (TME), which restores T-cell immune responses[30,31]. Meanwhile, JQ1 can abolish PD-L1 expression on the surface of the tumor cells by inhibiting bromodomain-containing protein 4 (BRD4)-involved transcription of the PD-L1 gene[32,33] (Fig. 1B).

2. Materials and methods

2.1. Materials

1-(3-Dimethylaminopropyl)-3-ethylcarbodiimide hydrochloride (EDCI), triethylamine (TEA), 4-dimethylaminopyridine (DMAP), *N*,*N*-diisopropylethylamine (DIEA), *N*,*N*-dimethylacetamide (anhydrous, DMAc), dimethyl sulfoxide (anhydrous, DMSO), *N*,*N*-dimethylformamide (anhydrous, DMF), dichloromethane (anhydrous, DCM), 2,2′-azobis (2-methylpropionitrile) were purchased from J&K Scientific Ltd. (Shanghai, China). Nile Red (NiR), 1,1′-dioctadecyl-3,3,3′,3′-tetramethylindocarbocyanine perchlorate (DiL) and 1,1′-dioctadecyl-3,3,3′,3′-tetramethyl indotricarbocyanineiodide (DiR) were all obtained from Life Technologies (Shanghai, China). NLG919 was purchased from Selleck Chemghai, China). PPa was purchased from Dibai Chem Tech Co., Ltd. (Shanghai, China). Triphosgene, 4-cyano-4-(dodecylsulfanylthiocarbonyl) sulfanylpentanoic acid (CTA) and bis(2-hydroxyethyl) disulfide were purchased from TCI (Shanghai, China). Enzyme-linked immunosorbent assay (ELISA) kits were ordered from Neobioscience Technology Co., Ltd. (Shenzhen, China). Kyn, Trp and 2,7-dichlorodihydrofluorescein diacetate (DCFH-DA) were ordered from Meilun Biotechnology Co., Ltd. (Dalian, China). The macromolecular chain transfer agent mPEG$_{113}$-CTA and 2-(hexamethyleneimino) ethanol methacrylate (HMA) were synthenzied by following the similar procedure reported previously[34,35].

2.2. Cell lines and animals

4T1 murine breast tumor cells and CT26 murine colorectal tumor cells were both supplied by the cell bank of Chinese Academy of

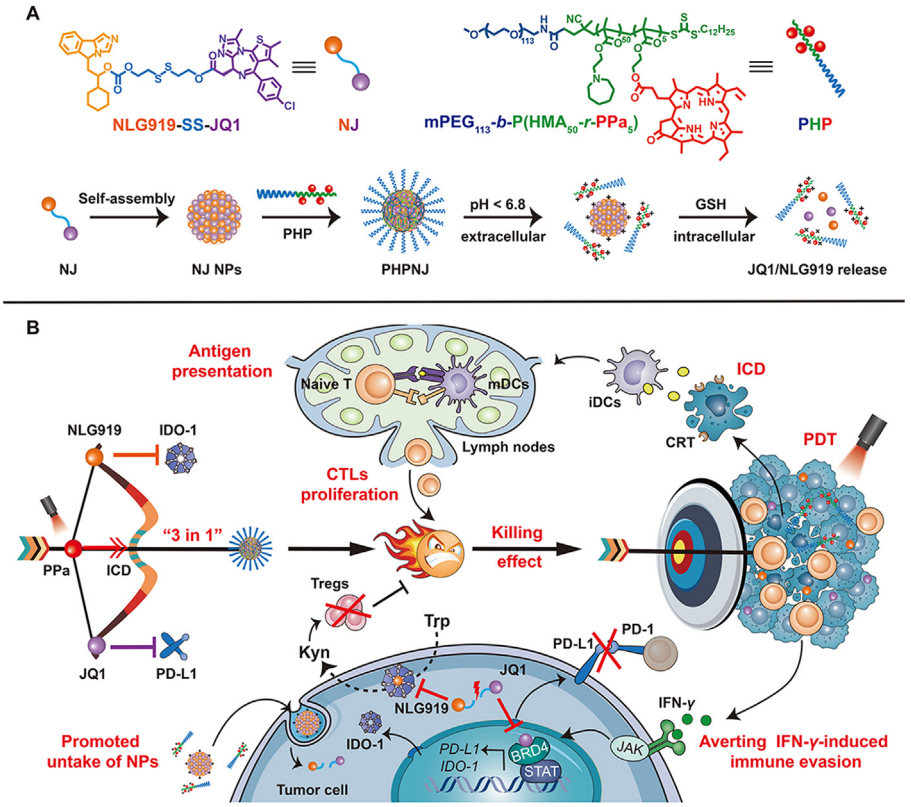

Figure 1 Schematic diagram for bispecific prodrug NPs-based combinatory immunotherapy of cancer by simultaneously overcoming multiple immune resistance mechanisms. (A) Self-assemble and tumor-specific activation of the bispecific prodrug NPs; (B) Proposed mechanisms of the prodrug NPs-based combinatory immunotherapy by eliciting immunogenicity and overcoming IDO-1/PD-L1-inducible adaptive immune resistance. Prodrug NPs-based PDT can combat the intrinsic immune resistance by initiating ICD of the tumor cells and recruiting the CTLs for tumor regression. Meanwhile, JQ1 and NLG919 released from the bispecific prodrug can relieve IFN-γ-induced adaptive immune resistance by impeding the transcription of PD-L1 with JQ1, and inhibiting IDO-1 activity with NLG919, respectively.

Sciences (Shanghai, China). Both types of cells were maintained in high-glucose Dulbecco's modified Eagle medium (DMEM) supplemented with 10% (*v*/*v*) of fetal bovine serum (FBS) and 1% penicillin-streptomycin. Both types of cells were incubated at 37 °C under a humidified atmosphere containing 5% of CO_2. All experiments were performed in the logarithmic phase of the cell growth.

BALB/c mice (female, 18−20 g, 4-week-old) were purchased from the Shanghai Experimental Animal Center (Shanghai, China). All animal procedures were conducted under the guidelines approved by the Institutional Animal Care and Use Committee (IACUC) of Shanghai Institute of Material Medica, Chinese Academy of Sciences (Shanghai, China).

2.3. *Synthesis of the prodrug dimers*

The heterogeneous dimer of NJ was synthesized by two-step reaction. First, triphosgene (207.9 mg, 0.7 mmol) in 10.0 mL DCM solution was added into 10.0 mL DCM solution of DMAP (389.4 mg, 3.2 mmol) and NLG919 (600.0 mg, 2.1 mmol). After 1.5 h of reaction under ice bath, the DCM solution of bis(2-hydroxyethyl) disulfide (492.8 mg, 3.2 mmol) was added, and the reaction was continued for 24 h. Then, the crude product was purified by silica gel chromatography to obtain NLG919-SS-OH with a yield of 86.3%. Second, JQ1-COOH (500.0 mg, 1.3 mmol), EDCI (382.0 mg, 2.0 mmol) and DMAP (244.0 mg, 2.0 mmol) were dissolved in DCM and reacted for 1.5 h under ice bath. Then, 10.0 mL DCM solution of NLG919-SS-OH (386.0 mg, 1.0 mmol) was added dropwise, and the reaction was continued for 24 h at room temperature. The crude product was purified by silica gel chromatography to obtain NJ dimer (yield 70.3%). The homogenous dimers of NLG919 (NLG919-SS-NLG919, DN) and JQ1 (JQ1-SS-JQ1, DJ) were synthesized by following the same procedure described above. The chemical structure and molecular weight of the dimers were examined by ^{1}H-NMR examination and electrospray ionization mass spectrometry (ESI-MS), respectively.

2.4. *Synthesis of $mPEG_{113}$-b-P(HMA_{50}-r-$HEMA_5$) diblock copolymer (PHMA)*

To synthesize diblock copolymer PHMA *via* the reversible addition−fragmentation chain transfer (RAFT) polymerization method, $mPEG_{113}$-CTA (200.0 mg, 0.037 mmol), HMA (553.8 mg, 2.60 mmol), HEMA (48.1 mg, 0.37 mmol) and AIBN (0.6 mg, 0.0037 mmol) were dissolved in 1.0 mL of DMF and the reaction was continued at 70 °C for 24 h under argon protection. The raw product was purified by dialyzing against deionized (DI) water and lyophilized to obtain PHMA diblock copolymer. The intracellular acid (*i.e.*, pH < 6.2)-responsible diblock copolymer of methoxy poly (ethylene glycol)$_{113}$-*b*-poly (2-diisopropylaminoethyl methacrylate)$_{50}$ ($mPEG_{113}$-*b*-$PDMA_{50}$, PDMA) was then synthesized by following the same procedure described above.

2.5. Synthesis of PPa-conjugated $mPEG_{113}$-b-P(HMA_{50}-r-$HEMA_5$) diblock copolymer (PHP)

$mPEG_{113}$-*b*-P(HMA_{50}-*r*-$HEMA_5$) (200.0 mg, 0.012 mmol) dissolved in 10.0 mL of DMF was added dropwise into 10.0 mL DMF solution of PPa (76.9 mg, 0.144 mmol), DMAP (35.1 mg, 0.288 mmol), EDCI (56.7 mg, 0.288 mmol), and DIEA (37.2 mg, 0.288 mmol) under ice bath. The reaction was continued for 24 h at room temperature, and the crude product was purified by dialyzing against DMSO and DI water and lyophilized to obtain the target product (yield 81.3%).

2.6. Fabrication and characterization of the prodrug NPs

To prepare the self-assembled prodrug NPs, 0.4 mg of NJ, DJ or DN were dissolved in 20.0 μL of DMSO and added into 1.0 mL of DI water under consistent stirring. Free dimers and DMSO were removed by ultracentrifugation (MWCO = 100 kDa).

To prepare polymer-coated prodrug NPs, 0.1 mg of PHP in 5.0 μL of DMAc was added into the suspension of above-mentioned prodrug NPs to obtain the polymer-coated prodrug NPs with a final concentration of 0.5 mg/mL, which were termed as PHPNJ, PHPDJ or PHPDN NPs respectively, according to the prodrug dimer used.

To investigate acidity/reduction-triggered dissociation, intracellular uptake and biodistribution of the prodrug NPs, the PHNJ NPs (coated with PHMA) were loaded with 20% (*w*/*w*) of NiR, DiL or DiR inside the hydrophobic core of the NPs. The resultant NPs were termed as PHNJ@NiR, PHNJ@DiL or PHNJ@DiR according to the fluorescence dye used, respectively.

2.7. Molecular docking

Intermolecular interactions of the prodrug dimers and intermolecular docking energy between JQ1 and NLG919 were predicted by molecular docking using AutoDock Vina 1.1.2 software. The docking scores were calculated to predict the affinity of self-dimerization. The final pose of every docking was selected from the top-scoring conformations.

2.8. The reduction and acidity sensitivity of the prodrug NPs in vitro

To verify the reduction and acid-sensitivity of the prodrug NPs, PHNJ NPs were incubated in four sets of buffer solutions (*i.e.*, 10 mmol/L of GSH at pH 7.4, 10 mmol/L of GSH at pH 6.5, GSH free at pH 7.4, and GSH free at pH 6.5) for determined time. The hydrodynamic diameter, polydispersity index (PDI) of size distribution, zeta-potential, and morphology of NPs were monitored by dynamic light scattering (DLS) and transmission electron microscopy (TEM), respectively.

To investigate acid and reduction-triggered release of JQ1 and NLG919, the prodrug NPs were incubated with four sets of buffer solutions as described above and dialyzed against the buffer solution to collect the released monomers. The monomer release rate was then examined by high-performance liquid chromatography (HPLC) analysis using xBridge C18 column (5.0 μm, 3 mm × 150 mm) with methanol/water as the elute (*v*/*v* = 9, flow rate of 0.5 mL/min).

2.9. Cellular uptake and intracellular distribution of the prodrug NPs in vitro

To investigate the impact of the acid-responsive ability of polymers on the cellular uptake profile of the bispecific prodrug NPs, 4T1 cells were seeded in the 24-well tissue culture plate at a density of 1.0×10^4 cells/well. Upon 24 h incubation, the cells were then treated with PHNJ@DiL or NJ@DiL for 1, 2 or 4 h at an identical DiL concentration of 5.0 μmol/L at pH 6.5 or pH 7.4. Afterwards, the cells that incubated under unequal conditions for various times were all stained with 4′,6-diamidino-2-phenylindole (DAPI) for 30 min and examined by confocal laser scanning microscopy (CLSM) (Leica, Germany) and flow cytometric measurement (FACS Calibur system, BD Biosciences, Oxford, UK).

2.10. The cytotoxicity and phototoxicity of the bispecific prodrug NPs in vitro

The cytotoxicity and phototoxicity of the prodrug NPs were measured using the CCK-8 assay. For cytotoxicity assay, 4T1 cells were seeded in the 96-well tissue culture plate at a density of 0.5×10^4 cells/well in 100.0 μL of medium for 12 h. The cells were incubated with bispecific prodrug NPs at different concentrations of NLG919 for 24 h. The cell viability was examined by CCK-8 assay.

To evaluate the phototoxicity of the NPs, 4T1 cells were incubated with the prodrug NPs at various PPa concentrations (0, 0.1, 0.2, 0.3 μg/mL) for 12 h and illuminated with a 671 nm laser (0, 100, 200, 400 mW/cm^2) for 2 min. The cells were continually cultured for 12 h and the cell viability was examined by CCK-8 assay.

2.11. PDT-induced ROS generation with the PHPNJ NPs in vitro

To monitor PDT-induced intracellular ROS generation *in vitro*, 4T1 cells were seeded in the 24-well tissue culture plate at a density of 1.0×10^4 cells/well and incubated overnight. These cells were then treated with NJ, PHPNJ at pH 7.4, or PHPNJ at pH 6.5 (at an identical PPa concentration of 0.3 μg/mL). The cells treated with PHPNJ at pH 7.4, or PHPNJ at pH 6.5 were pre-stained with DCFH-DA for 30 min and then illuminated with 671 nm laser for 1 min at photodensity of 400 mW/cm^2. PDT-induced ROS generation was then examined by CLSM and flow cytometric measurement. The cell group incubated with PHPNJ at pH 7.4 with or without laser irradiation was named as $PHPNJ^{L/pH\ 7.4}$ and PHPNJ, respectively. In contrast, the cells incubated with PHPNJ at pH 6.5 with laser irradiation was named as $PHPNJ^{L/pH\ 6.5}$.

2.12. PDT-induced ICD in vitro

PDT-induced ICD effect *in vitro* was investigated by examining calreticulin (CRT) expression on the surface of the tumor cells, 4T1 cells were seeded in 24-well tissue culture plate at a density of 5.0×10^4 cells/well. The cells were then treated with different conditions for 24 h (*i.e.*, PBS, NJ, PHPNJ, $PHPNJ^{pH\ 7.4}$, $PHPNJ^{pH\ 6.5}$, at an identical PPa concentration of 0.3 μg/mL). The cells were then illuminated with 671 nm laser for 1 min at photodensity of 400 mW/cm^2 and continually cultured for 4 h. CRT expression on the

surface of the tumor cells were then analyzed by flow cytometric and CLSM measurements, respectively. The cell group incubated with PHPNJ at pH 7.4 and pH 6.5 with laser irradiation were named as $PHPNJ^{L/pH\ 7.4}$ and $PHPNJ^{L/pH\ 6.5}$, respectively.

2.13. *DC maturation in vitro*

To stimulate DC maturation by the bispecific prodrug NPs, the bone marrow-derived monocytes (BMDMs) isolated from 6 to 8 weeks old BALB/c mice were differentiated into $CD11c^{+}$ bone marrow-derived dendritic cells (BMDCs) with interleukin-4 (20.0 ng/mL) and mouse recombinant granulocyte-macrophage colony stimulating factor (20.0 ng/mL). Starting on the fourth day of the maturation process, 4T1 cells were seeded in the 24-well tissue culture plate at a density of 5.0×10^4 cells/well and were pretreated with five experimental groups (at an identical PPa concentration of 0.3 μg/mL). The tumor cells were then irradiated with 671 nm laser (400 mW/cm^2) for 1 min and co-cultured with the pre-mature BMDCs. The frequency of matured BMDCs was then determined by flow cytometry measurement.

2.14. *Western blot assay*

To investigate IFN-γ-induced acquired immune tolerance and verify PD-L1 downregulation by the bispecific prodrug NPs, Western blot (WB) assay was used to examine PD-L1 and IDO-1

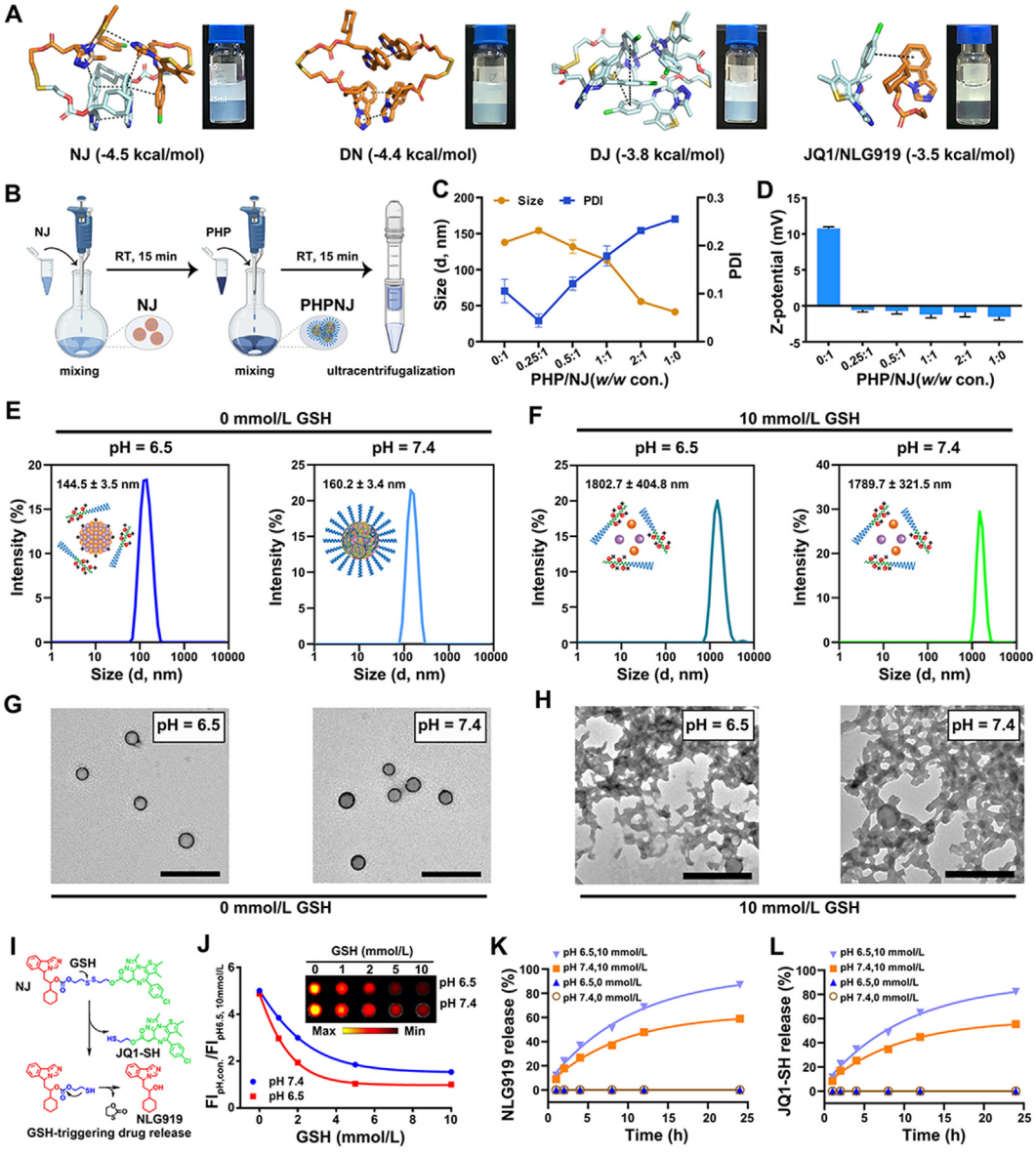

Figure 2 Physicochemical characterization of the bispecific prodrug NPs. (A) Docking models, predicted binding affinities and suspensions of the NJ, DN, DJ dimers and physical mixture of NLG919 and JQ1; (B) Schematic diagram for the preparation of the PHPNJ NPs; (C) Particle size, and (D) surface charge changes of the prodrug NPs as a function of PHP to NJ mass ratio; (E, F) Hydrodynamic size distribution in (E) GSH-free, and (F) 10 mmol/L GSH solution at pH 6.5 or 7.4; (G, H) The representative TEM images of the PHPNJ NPs in (G) GSH-free and (H) 10 mmol/L GSH at pH 6.5 or 7.4 (scale bars = 500 nm); (I) Schematic diagram of GSH-triggered reduction of the disulfide bond and release of NLG919 and JQ1 from the NJ dimer; (J) The fluorescence change of NiR-labelled PHNJ@NiR NPs upon 12 h of incubation at pH 7.4 or 6.5 with the addition of GSH; (K) NLG919 and (L) JQ1-SH release profiles of PHPNJ NPs.

expression in various groups. 4T1 and CT26 cells were seeded in 6-well tissue culture plates at cell density of 1.5×10^5 cells/well and 3.0×10^5 cells/well, respectively. The cells were then treated with IFN-γ, NLG919, JQ1 or various prodrug NPs (at an identical JQ1 dose of 500 nmol/L and NLG919 dose of 4.0 μg/mL, respectively). The cells were then lysed with RIPA lysis buffer containing 1% protease inhibitor. The target protein expression was analyzed by WB assay and semi-quantitatively analyzed by Image J software (NIH, USA).

2.15. *Pharmacokinetics profiles of the prodrug NPs in vivo*

To investigate the pharmacokinetics of the prodrug NPs, BALB/c mice were intravenously (i.v.) injected with NJ or PHNJ NPs at an identical JQ1 dose of 15.0 mg/kg and NLG919 dose of 10.0 mg/kg. Blood samples were collected at predetermined time points post-injection (*e.g.*, 5, 20 min, 1, 4, and 12 h) and quickly centrifuged to get the upper layer of plasma. The serum contents of JQ1 and NLG919 were then examined by HPLC measurement.

2.16. *Biodistribution and tumor penetration of the prodrug NPs in vivo*

To investigate the tissue distribution and tumor penetration profiles of the prodrug NPs *in vivo*, 4T1 breast tumor model was established by subcutaneously (s.c.) injecting 1.0×10^6 4T1 cells on the right mammary gland. The 4T1 tumor-bearing BALB/c mice at tumor volume of 200 mm^3 were i.v. injected with PHNJ@DiR or PDNJ@DiR at an identical NLG919 dose of 10.0 mg/kg and JQ1 dose of 15.0 mg/kg, respectively. Near-infrared fluorescence imaging were then performed *in vivo* and *ex-vivo* at predetermined time points post-injection (*e.g.*, 2, 4, 8, 12, 24 or 48 h) by using an IVIS Imaging System (Spectrum CT, PerkinElmer, USA).

2.17. *Anti-tumor performance of the bispecific prodrug NPs in vivo*

To explore the antitumor activity of the PHPNJ NPs *in vivo*, the 4T1 murine breast tumor model and CT26 colorectal tumor model were established by s.c. injecting 4T1 tumor cells on the right mammary gland and CT26 tumor cells in the right flank of the BALB/c mice, respectively. The 4T1 and CT26 tumor-bearing mice were randomly divided into five groups ($n = 5$) when the tumor volume reached ~50 mm^3. The tumor-bearing mice were then treated with PBS, PHPNJ, PHPDN, or PHPDJ at an identical NLG919 dose of 10.0 mg/kg and JQ1 dose of 15.0 mg/kg, respectively. The PHPDN, PHPDJ and PHPNJ groups were selectively irradiated with 671 nm laser at photodensity of 600 mW/cm^2 for 10 min at the time point 12 h post-injection (termed as $PHPDN^L$, $PHPDJ^L$ and $PHPNJ^L$, respectively). The final five kinds of treatments (*i.e.*, PBS, PHPNJ, $PHPDN^L$, $PHPDJ^L$ and $PHPNJ^L$) were repeated for five times at an interval of three days. The tumor growth curves were monitored and recorded every other day, and the tumor volume was calculated by Eq. (1):

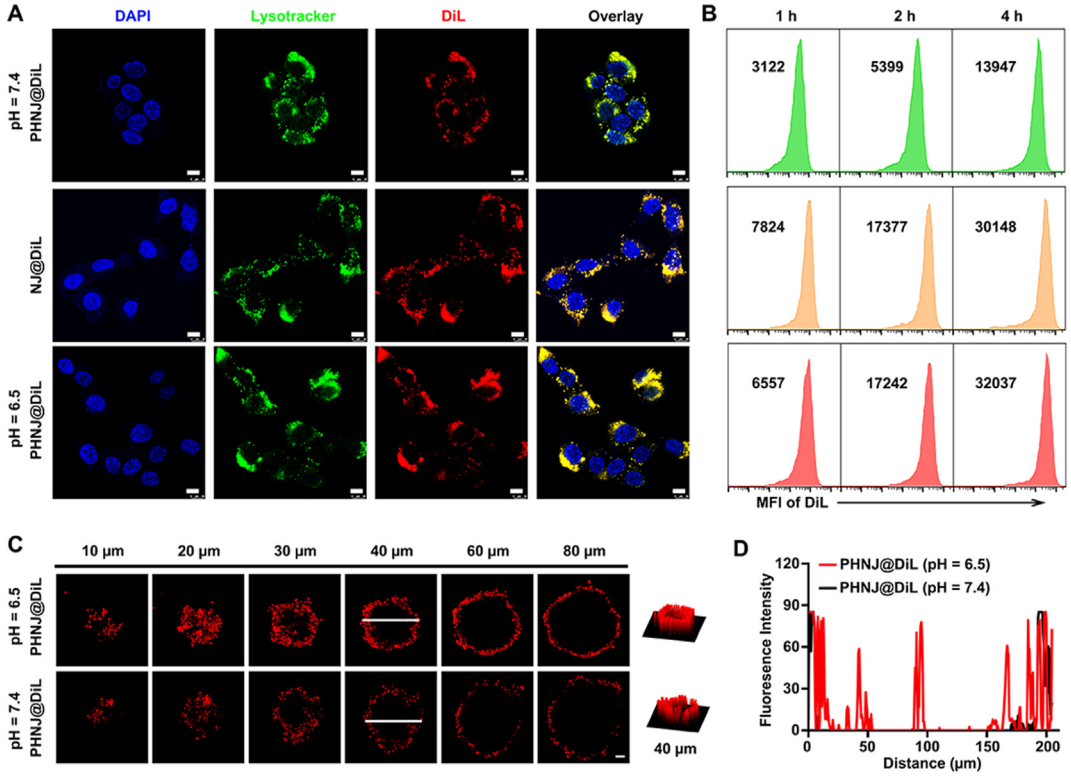

Figure 3 Cellular uptake and tumor penetration properties of the prodrug NPs *in vitro*. (A) The representative CLSM images (scale bar = 10 μm), and (B) Flow cytometric plots of intracellular uptake of the PHNJ@DiL or NJ@DiL NPs in 4T1 breast tumor cells *in vitro* (treated at an identical DiL concentration of 5.0 μmol/L); (C) CLSM examination of tumor penetration profile of the prodrug NPs in the 3-D spheroids of 4T1 tumor upon 8 h incubation *in vitro* (scale bar = 50 μm); (D) Quantitative fluorescence intensity profile along the arrow region at depth of 40 μm.

$$V = L \times W \times W/2 \quad (1)$$

where L represents the longest dimension, W represents the shortest dimension.

The mice were pronounced death once the tumor volume reached 3500 mm^3. The tumor and the major organs (*i.e.*, heart, liver, lung, spleen, and kidneys) were harvested at the end of antitumor studies and fixed in 4% formalin solution. The tumor and the major organs were then examined by Hematoxylin-Eosin (H&E) staining.

2.18. Immune analysis in vivo

To analyze the immune response inducted by the bispecific prodrug NPs, mice bearing 4T1 tumors of approximately 120 mm^3 were treated with PHPNJ, PHPDN, or PHPDJ at an identical NLG919 dose of 10.0 mg/kg and JQ1 dose of 15.0 mg/kg, respectively. The tumors in the PHPNJ, PHPDN, and PHPDJ groups were irradiated with 671 nm laser at 600 mW/cm^2 for 10 min at 12 h post-injection. There were five groups in total, termed as PBS, PHPNJ, $PHPDN^L$, $PHPDJ^L$ and $PHPNJ^L$, respectively. The treatments were repeated triplicates at a time interval of three days. All the tumor tissues and the tumor-draining lymph nodes (LNs) were collected for flow cytometry and immunohistology examination of the immune cells. IFN-γ secretion in the tumor tissue was examined by ELISA measurement.

2.19. Statistical analysis

Statistical analysis was performed using GraphPad Prism 8.0. All the data were presented as mean ± SD. Unpaired two-tailed *t*-test was used to determine the significance of the difference between two sets of data. The parametric test with Welch's correction was used if both populations have unequal SDs. The P values in the survival curve were obtained by Logrank test. Statistical significance was set at $^{*}P < 0.05$, $^{**}P < 0.01$, $^{***}P < 0.001$, $^{****}P < 0.0001$.

3. Results and discussion

3.1. Fabrication and characterization of the prodrug NPs

To fabricate the bispecific prodrug NPs, we first synthesized a set of prodrugs of NLG919 and JQ1 *via* a disulfide bond spacer (*e.g.*, NJ, DN and DJ, Supporting Information Figs. S1–S3). The chemical structure and molecular weight of the three prodrug dimers were validated by ^{1}H-NMR examination and ESI-MS (Supporting Information Figs. S4–S9), respectively.

The tumor acidity-ionizable diblock copolymer PHMA was synthesized *via* RAFT polymerization procedure as reported previously[34]. The composition of the resultant diblock copolymer was identified as $mPEG_{113}$-*b*-P(HMA_{50}-*r*-$HEMA_5$) by ^{1}H-NMR

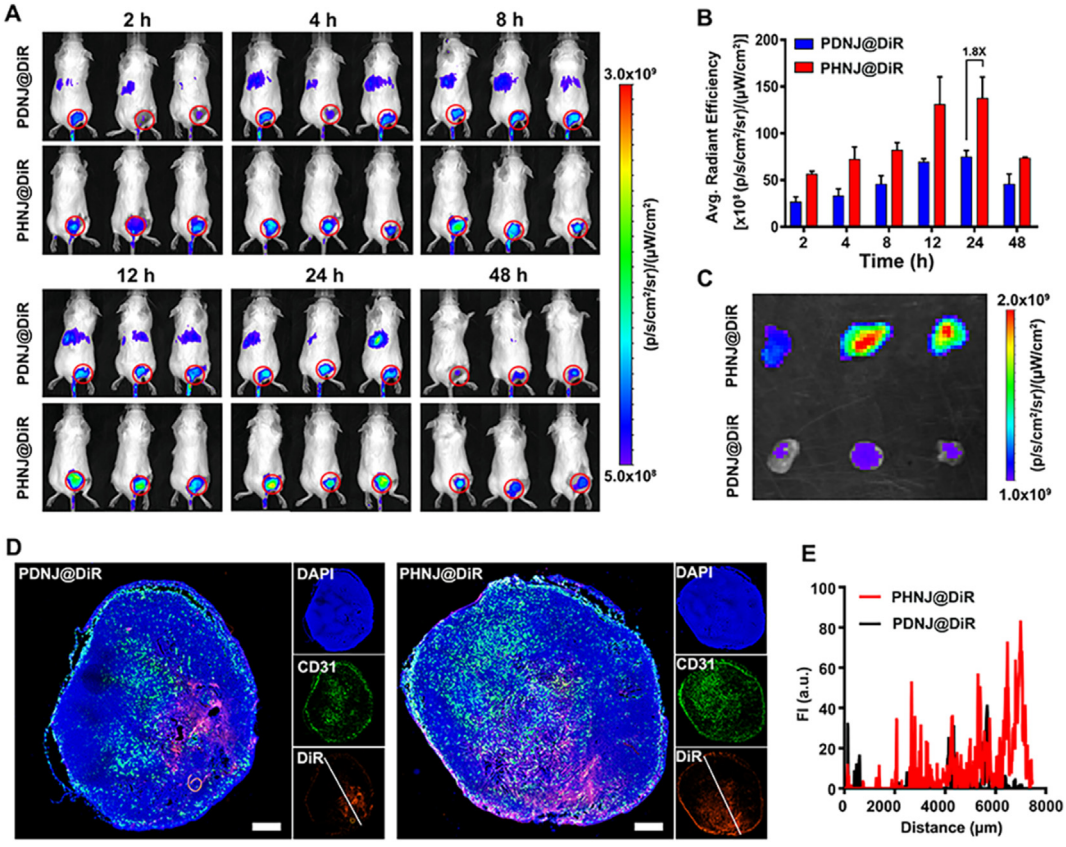

Figure 4 Tumor microenvironment extracellular acidity enhanced tumor penetration and accumulation of bispecific prodrug NPs *in vivo*. (A) Fluorescence imaging of prodrug NPs PDNJ@DiR or PHNJ@DiR distribution in 4T1 tumor-bearing mice *in vivo* (PDNJ@DiR or PHNJ@DiR was i.v. injected at an identical DiR dose of 0.2 mg/kg); (B) Semi-quantitative analysis of fluorescence distribution in the tumor tissue; (C) *Ex-vivo* fluorescence imagining of nanoparticle distribution in the tumor mass *ex-vivo* at 24 h post-injection; (D) CLSM examination of NPs distribution in the 4T1 tumor sections *ex-vivo* at 24 h post-injection, and (E) semi-quantitative analysis of fluorescence intensity in the tumor section *ex-vivo* (scale bar = 1.0 mm).

spectra (Supporting Information Figs. S10–S16). PPa was then conjugated on the pendant hydroxyl groups of PHMA to obtain the final copolymer PHP with five PPa molecules on each polymer chain (Supporting Information Figs. S17 and S18).

To evaluate the self-assemble property of the dimeric prodrugs, we first calculated the intermolecular docking energy of NJ, DN, DJ, and the intermolecular docking energy between free JQ1 and NLG919 (Fig. 2A). All three dimers (NJ, DN and DJ) displayed much lower docking energy than that of free JQ1 and NLG919, indicating higher thermal stability of self-assemble dimer NPs than the randomly mixed JQ1/NLG919. The suspension of the dimeric NPs kept stable upon 24 h storage, which were all prepared by the two-step dropping method (Fig. 2A and B). In contrast, the physical mixture of JQ1 + NLG919 deposited immediately upon water dilution, verifying good colloidal stability of the prodrug NPs due to the disulfide effect[36,37].

The formulations of PHP-coated NJ NPs (termed as PHPNJ) were then optimized by screening the hydrodynamic diameter and PDI of particle size distribution (Fig. 2C). The PHPNJ NPs prepared at PHP to NJ mass ratio of 0.25:1 showed a hydrodynamic diameter around 150 nm and the narrowest PDI as determined by DLS analysis, which was used throughout this study. The resultant PHPNJ NPs displayed neutral surface charge (~0.6 mV, Fig. 2D), verifying surface coating of NJ NPs with the polymer shell. Several other kinds of polymer-coated DN and DJ NPs were also prepared at the polymer to dimer mass ratio of 0.25:1 (namely PHPDN and PHPDJ) and used as the control NPs (Supporting Information Table S1).

The self-assembled PHPNJ NPs showed high drug-loading efficiency (~37.8% (*w*/*w*) for JQ1 and ~26.7% (*w*/*w*) for NLG919, respectively) for minimizing the use of excipient[38]. Furthermore, the polymer-coated PHPNJ NPs exhibited good colloidal stability upon 10-days storage in FBS solution (10% *w*/*w*) (Supporting Information Fig. S19), which could be attributed to the hydrophobic interaction between the PHP shell and the NJ core.

The acid and reduction sensitivity of the PHPNJ NPs were next examined by TEM and DLS measurements. The PHPNJ NPs were incubated in PBS solution at pH 6.5 to mimic the extracellular acidity of the TME. Upon 12 h incubation at pH 6.5, the particle size of the PHPNJ NPs decreased from 160.2 to 144.5 nm. In contrast, PHPNJ NPs kept stable at pH 7.4 (Fig. 2E). The decreased particle size in the acidic buffer solution could be explained by acid-triggered detachment of the PHP shell from the PHPNJ NPs. Of note, the polymer-coated prodrug NPs swelled dramatically in 10 mmol/L of GSH solution at pH 7.4 or 6.5 due to GSH-triggered reduction of the NJ dimer and dissociation of the NJ core (Fig. 2F). TEM examination of the NP morphology displayed amorphous aggregates upon acid/GSH incubation, which further validated GSH-triggered dissociation of the prodrug NPs (Fig. 2G and H).

GSH-triggered NLG919 and JQ1 release inside the tumor cells was crucial for inactivating IDO-1 and BRD4 for combating the adaptive immune resistance of the tumor (Fig.

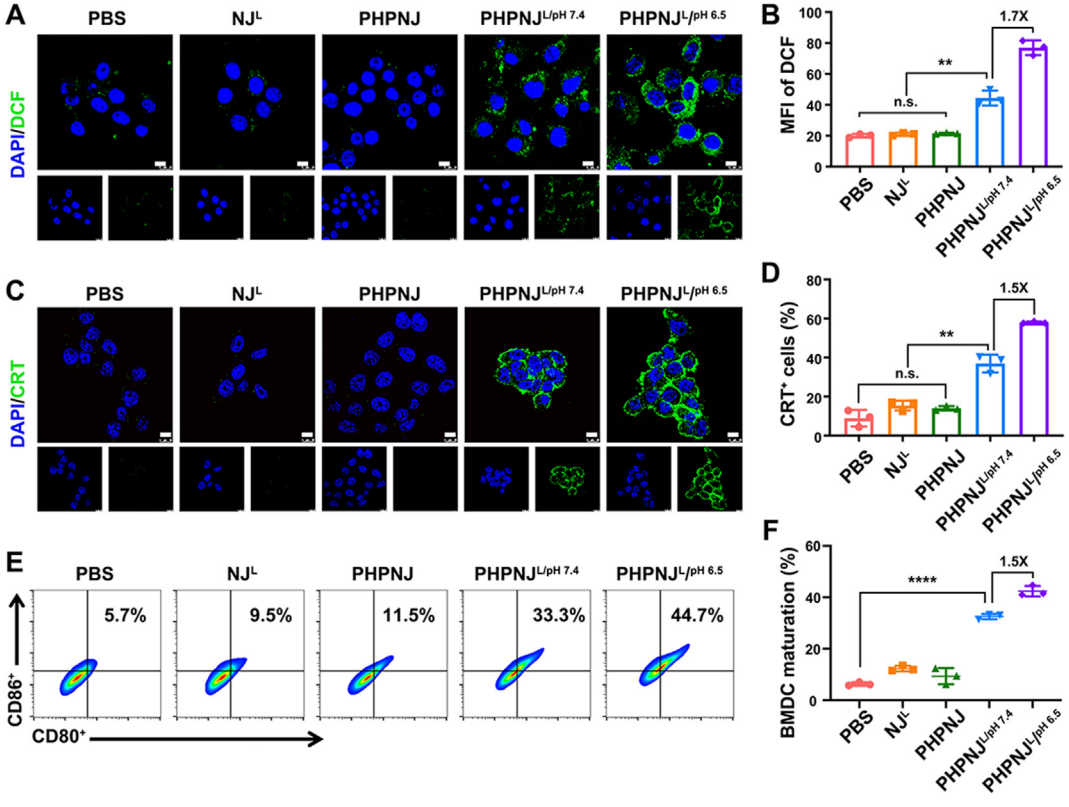

Figure 5 PHPNJ NPs circumvented the intrinsic immune evasion by eliciting immunogenicity of the tumor cells *in vitro*. (A) CLSM examination (scale bar = 10 μm), and (B) flow cytometric measurement of PDT-triggered ROS generation in 4T1 cells post diverse treatments at an identical PPa concentration of 0.3 μg/mL; (C) CLSM examination of PDT-induced CRT translocation on surface of 4T1 cells (scale bar = 10 μm), and (D) flow cytometry measurement of CRT^+ cells by different treatments; (E) Representative flow cytometric plots, and (F) the averaged BMDC maturation ratio (gated on $CD11c^+CD80^+CD86^+$) stimulated by NPs-treated 4T1 cells *in vitro* ($n = 3$). The data were showed as mean ± SD. $^{**}P < 0.01$; $^{***}P < 0.001$; $^{****}P < 0.0001$; n.s., not significant.

2I). To confirm the reduction-triggered drug release from the prodrug NPs, the polarity-sensitive fluorescence dye NiR was loaded into PPa-free PHNJ NPs and incubated with different concentrations of GSH in pH 6.5 and pH 7.4 buffer for 12 h. Fluorescent imaging showed that the fluorescence of NiR declined gradually as a function of GSH concentration due to NiR release from the hydrophobic core into the aqueous solution (Fig. 2J). The weakest fluorescent signal with 10 mmol/L GSH also represented that almost NiR dye was sufficiently released from PHNJ NPs with 10 mmol/L GSH in pH 6.5 or 7.4 buffer. Under the same GSH concentration, the faster fluorescence quenching of NiR in pH 6.5 buffer meant faster dissociation of PHNJ NPs, which benefited from tumor-activatable detachment of PHMA corona from NJ NPs core (Fig. 2J).

We next investigated the drug release profile of the PHPNJ NPs by HPLC. As showed in Fig. 2K and L, without the addition of GSH, NLG919 and JQ1 were marginally released from the PHPNJ NPs upon 24 h incubation at pH 6.5 or 7.4. In contrast, around half of NLG919 and JQ1 were released upon 24 h incubation in 10 mmol/L of GSH solution at pH 7.4. Increased drug release was achieved (*i.e.*, 86.9% of NLG919 and 82.2% of JQ1, respectively) within 24 h when incubated in 10 mmol/L of GSH solution at pH 6.5 (Fig. 2K, L and Supporting Information Fig. S20). These phenomena suggested the crucial roles of tumor acidity and reduction microenvironment for activating the prodrug drugs.

3.2. *Acidity-triggered cellular uptake of the prodrug NPs in vitro*

Given the superior acidity and reduction-sensitivity of the prodrug NPs, we next investigated their cellular uptake profile *in vitro*. For this purpose, DiL-labelled prodrug NPs were prepared by encapsulating DiL dye inside the hydrophobic core of the prodrug NPs. CLSM examination displayed that the prodrug NPs were efficiently internalized with the tumor cells and colocalized with the lysosome vesicles (Fig. 3A).

Noticeably, in comparison with that of the PHNJ@DiL group incubated at pH 7.4, flow cytometry examination revealed much more cellular uptake of the PHNJ@DiL prodrug NPs in the 4T1 cells when incubated at pH 6.5, mimicking the tumor acidic microenvironment (Fig. 3B). The increased cellular uptake of the prodrug NPs could be explained by acidity-triggered detachment of the polymer shell, which has been well identified for restricting cellular interaction of the NPs[39].

Given the increased cellular uptake of the prodrug NPs at acidic condition, we next sought to investigate their tumor penetration profile using 3-D tumor spheroids *in vitro*. CLSM examination showed that the PHNJ@DiL NPs penetrated much more deeply into the tumor spheroids when incubated at pH 6.5 compared to that examined at pH 7.4, which could be attributed to extracellular acidity-triggered cleavage of the PHMA shell (Fig. 3C and D).

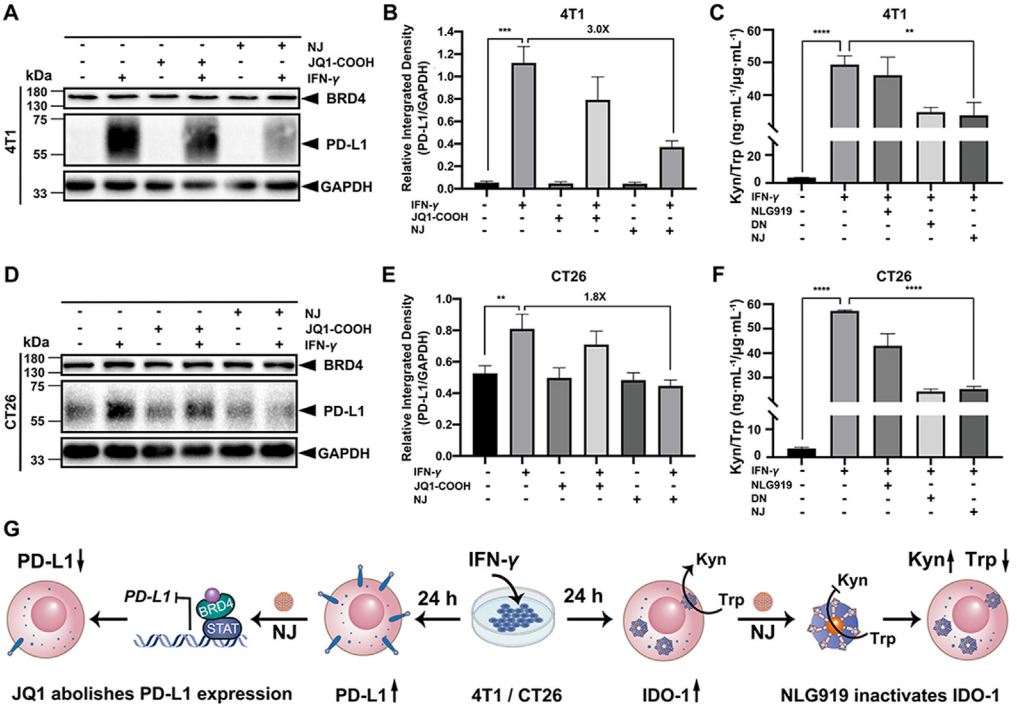

Figure 6 PHPNJ NPs circumvented IFN-γ-inducible adaptive immune resistance *in vitro*. (A) WB assay of IFN-γ-elicited PD-L1 expression in the 4T1 cells *in vitro*, which was abolished by JQ1 and NJ prodrug (the cells were co-incubated with IFN-γ (100 ng/mL) and JQ1 or NJ prodrug (at an identical JQ1 concentration of 500 nmol/L) for 24 h and continually treated with JQ1 or NJ NPs for additional 24 h); (B) Semi-quantitative analysis of WB assay-determined PD-L1 expression in 4T1 cells by Image J software ($n = 3$); (C) HPLC examination of IFN-γ-inducible IDO-1 overactivation and NLG919-mediated IDO-1 inactivation in 4T1 cells *in vitro* ($n = 3$); (D) WB assay of IFN-γ-inducible and NJ-abolished PD-L1 expression; (E) Semi-quantitative analysis of WB assay-determined PD-L1 expression in CT26 cells *in vitro* ($n = 3$); (F) HPLC examination of IFN-γ-inducible IDO-1 overactivation and NLG919-mediated IDO-1 inactivation in CT26 cells ($n = 3$) (an identical IFN-γ concentration of 100 ng/mL and NLG919 concentration of 4.0 μg/mL, respectively); (G) Schematic diagram of NJ-mediated blockade of IFN-γ-inducible PD-L1 and IDO-1 upregulation in 4T1 and CT26 cells. The data were showed as mean ± SD. $^{**}P < 0.01$; $^{***}P < 0.001$; $^{****}P < 0.0001$; n.s., not significant.

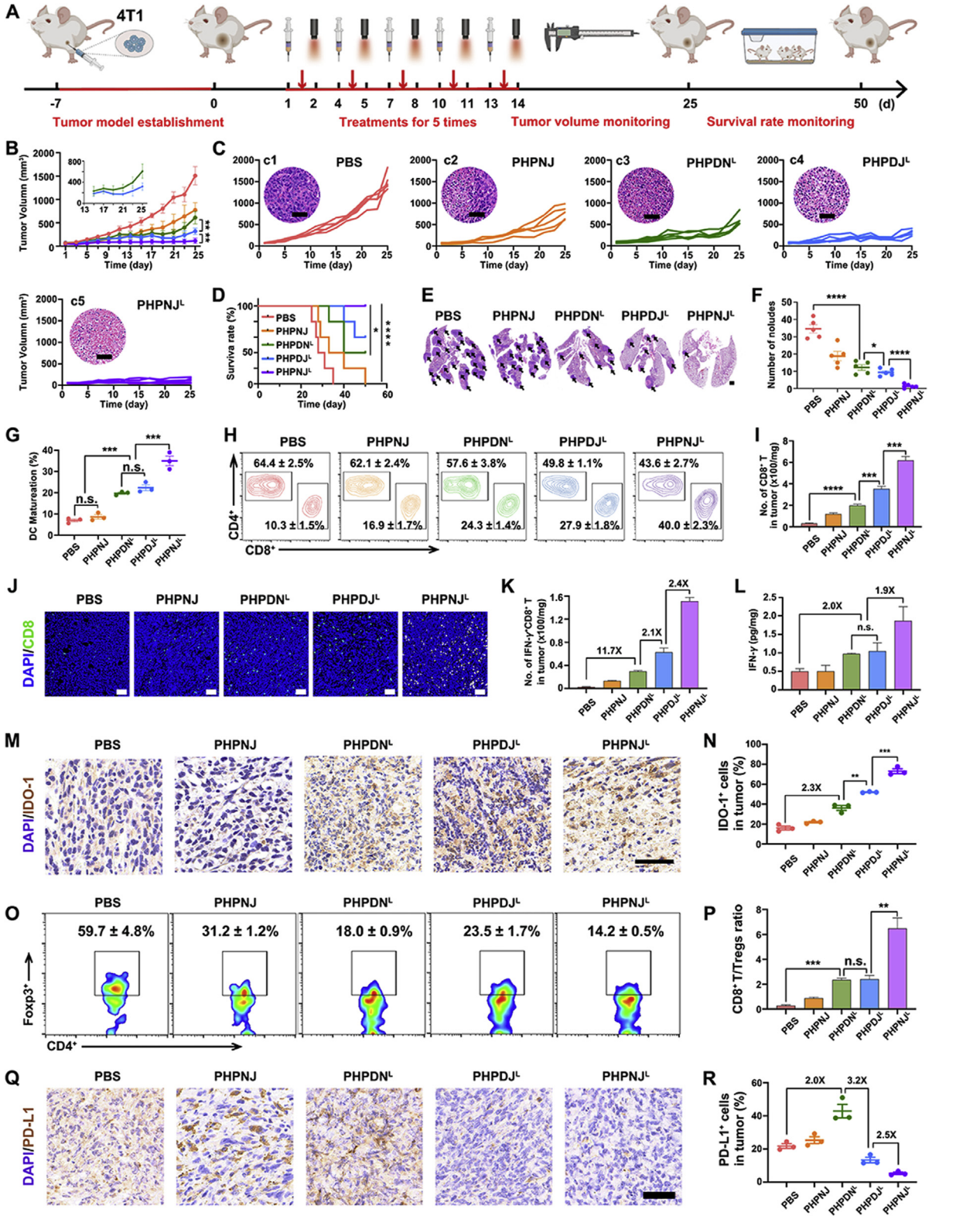

Figure 7 Anti-tumor performance of the bispecific prodrug NPs in 4T1 breast tumor model. (A) Treatment schedule for prodrug NPs-mediated combinatory immunotherapy at an identical JQ1 dose of 15.0 mg/kg, and NLG919 dose of 10.0 mg/kg; (B) The averaged tumor growth profiles of 4T1-tumor-bearing mice upon various treatments ($n = 5$), and (C) the individual tumor growth curves of the 4T1 tumor-bearing mice (the inserts showed the representative H&E images of the tumor sections, scale bar = 60 μm); (D) Survival curves of the 4T1 tumor-bearing mice monitored for 50 days ($n = 5$); (E) The representative H&E images of the lung sections (scale bar = 1 mm), and (F) the number of the pulmonary metastasis nodules examined at the end of the antitumor studies ($n = 5$); (G) DC maturation in the tumor-draining LNs following different treatments and examined 5th day post-injection ($n = 3$); (H) Representative flow cytometric plots of the tumor-infiltrating $CD8^+$ and $CD4^+$ T cell population;

3.3. Biodistribution and tumor penetration of the prodrug NPs in vivo

To investigate the pharmacokinetic property of the bispecific prodrug NPs *in vivo*, the plain NJ NPs and PHMA-coated PHNJ NPs were both i.v. injected into the BLAB/c mice, and then the blood concentration of the NJ dimer was examined by HPLC measurements (Supporting Information Fig. S21). PHNJ NPs displayed much higher bioavailability than that of the NJ NPs, suggesting that surface coating of the NJ NPs with PHMA diblock copolymer significantly elongated the blood circulation of the NJ prodrug.

To further investigate the effect of the tumor acidity-activatable PHMA shell for tumor-specific delivery and deep tumor penetration of the NJ prodrug *in vivo*, we prepared the PDNJ@DiR NPs composed of intracellular acidity (pH < 6.2)-responsive PDMA shell as the control[40]. The 4T1 tumor-bearing BLAB/c mice were i.v. injected with the PDNJ@DiR or PHNJ@DiR NPs and then examined using near-infrared fluorescence imaging *in vivo* at the pre-determined time points post-injection. Fig. 4A showed that both PDNJ@DiR and PHNJ@DiR NPs gradually accumulated at the tumor site *via* the enhanced permeability and retention (EPR) effect in a time-dependent manner. Tumor distribution of the prodrug NPs reached the peak at 24 h post-injection and declined slightly at 48 h post-injection, due to blood clearance of the DiR dye from the tumor (Fig. 4B). Noticeably, the PHNJ@DiR group showed 1.8-fold higher tumoral fluorescence intensity than PDNJ@DiR control group, suggesting increased tumor accumulation of the PHNJ@DiR prodrug NPs as validated by fluorescence imaging of the tumor tissue *ex-vivo* (Fig. 4C).

To demonstrate the advantage of the PHMA shell for promoting tumor-specific delivery of the NJ prodrug, the tumor tissues were frozen sectioned and examined by CLSM measurement. Fig. 4D displayed that the PDNJ@DiR NPs were dominantly distributed in the perivascular areas without noticeable diffusion inside the tumor tissue. In contrast, the PHNJ@DiR NPs showed highly diffused pattern and brighter fluorescence signal than that of the PDNJ@DiR NPs group. Semi-quantitative examination of the intratumoral fluorescence intensity further verified increased tumor distribution and deep tumor penetration of the PHNJ@DiR NPs (Fig. 4E).

In previous studies, we had developed several sets of tumor-acidic or enzymatic (*e.g.*, matrix metalloproteinases, MMPs)-responsive nanoparticles for promoting tumor accumulation and retention[41]. Given the tumor acidity-responsive property of the PHMA diblock copolymer, the highly increased tumor distribution and deep penetration profiles of the PHNJ@DiR NPs could thus be explained by tumor acidity-triggered deshielding of the polymer shell.

3.4. Prodrug NPs circumventing intrinsic immune resistance in vitro

Given the superior tumor acidity-responsive property of the prodrug NPs for achieving efficient cellular uptake and tumor-specific distribution, we next investigated their potential for eliciting antitumor immunogenicity to overcome the intrinsic immune resistance. The prodrug NPs displayed negligalbe influence on the cell viability at a drug concenrtration up to 10 μmol/L (Supporting Information Fig. S22). Therefore, a prodrug concentration (at an identical JQ1 concentration less than 10 μmol/L) was selected for the subsequent cell culture studies *in vitro*. The photoactivity of the PHPNJ NPs was then evaluated in 4T1 cells *in vitro* by using DCFH-DA as a fluorescent probe of ROS. CLSM examination showed that upon 671 nm laser irradiation at 400 mW/cm^2, PHPNJ$^{L/pH\ 7.4}$ and PHPNJ$^{L/pH\ 6.5}$ group induced significant ROS generation in the 4T1 tumor cells *in vitro* (Fig. 5A). Noticeably, intracellular ROS generation increased further by 1.7-fold higher than that of the PHPNJ$^{L/pH\ 7.4}$ group when incubated at acidic pH of 6.5 (Fig. 5B and Supporting Information Fig. S23A). This phenomenon could be explained by increased cellular uptake of the PHPNJ NPs at acidic condition (Fig. 3A). The PHPNJ NPs displayed noticeable photocytotoxicity in 4T1 tumor cells as a function of PPa-concentration and photodensity due to PDT-induced ROS generation in the tumor cells *in vitro* (Supporting Information Fig. S24).

CRT is a proapoptotic protein located in the endoplasmic reticulum, which translocates to the surface of the cell membrane when the tumor cells undergoing ICD[42]. To evaluate PDT-induced ICD of the tumor cells *in vitro*, CRT expression on the surface of the tumor cells was examined by CLSM measurement and flow cytometric assay, respectively. CLSM examination showed negligible CRT expression on the surface of the tumor cells of the NJ^L and PHPNJ groups (Fig. 5C). In contrast, tumor cells treated with PHPNJ$^{L/pH\ 7.4}$ dramatically elicited CRT translocation to membrane, and the proportion of the CRT$^+$ cells further increased by 1.5-fold when incubated at pH 6.5 (Fig. 5D and Fig. S23B), verifying a positive correlation between laser irradiation-induced ROS generation and ICD effect.

To demonstrate the potential of the prodrug NPs for inducing antitumor immune response, we next evaluated whether PHPNJ-mediated ICD could potentiate DC maturation *in vitro*. Briefly, the BMDCs were freshly separated from BALB/c mice and incubated with the pretreated tumor cells for 24 h. Results showed that the tumor cells pretreated with PHPNJ$^{L/pH\ 7.4}$ and PHPNJ$^{L/pH\ 6.5}$ significantly increased the frequency of matured DCs (Fig. 5E). For instance, the DC maturation ratio in the PHPNJ$^{L/pH\ 6.5}$ group was 1.5-fold higher than that of the PHPNJ$^{L/pH\ 7.4}$ group, due to increased PDT efficacy and CRT exposure ratio at pH 6.5 (Fig. 5F). These CRT expression and DC maturation data consistently validated the potential of the prodrug NPs for inducing immune response and thus circumventing intrinsic immune resistance.

3.5. Prodrug NPs overcoming adaptive immune resistance in vitro

We next investigated whether the prodrug NPs could relieve IFN-γ-inducible adaptive immune resistance by suppressing PD-L1

(I) The tumor mass-normalized tumor-infiltrating CD8$^+$ T cells examined at 5th day post-injection; (J) Immunofluorescence staining of the tumor-infiltrating CD8$^+$ T lymphocytes in the 4T1 tumor sections at 5th day post the final treatments (scale bar = 50 μm); (K) Tumor mass-normalized tumor-infiltrating IFN-γ$^+$CD8$^+$ T cells and (L) ELISA examination of intratumoral IFN-γ secretion (n = 3); (M) IHC examination of IDO-1 expression (scale bar = 50 μm); (N) Semi-quantitative analysis of IDO-1 expression in the tumor sections of 4T1 tumor at the end of the antitumor study; (O) Flow cytometric analysis of the tumor-infiltrating Tregs and (P) the ratio of the tumor-infiltrating CD8$^+$ T cells to Tregs examined at 5th day post treatment (n = 3); (Q) IHC examination of PD-L1 expression (scale bar = 50 μm), and (R) Semi-quantitative analysis of PD-L1 expression in the 4T1 tumor sections at the end of the antitumor study. The data were showed as mean ± SD. *P < 0.05; **P < 0.01; ***P < 0.001; ****P < 0.0001; n.s., not significant.

expression with JQ1, and inhibiting IDO-1-mediated Trp metabolism with NLG919, respectively. The 4T1 and CT26 tumor cells were first treated with IFN-γ for 24 h, and then incubated with the NJ NPs for additional 24 h and examined for PD-L1 expression and IDO-1 activity by WB and HPLC assay, respectively. WB assay showed that IFN-γ dramatically elicited PD-L1 and IDO-1 expression inside the tumor cells in an IFN-γ concentration-dependent manner (Supporting Information Figs. S25 and S26). Noticeably, IFN-γ-inducible PD-L1 expression was almost completely abolished by NJ NPs (Fig. 6A and B), verifying that JQ1 was effectively released from the NJ prodrug *via* GSH-mediated cleavage of the disulfide bond in the tumor cells.

IDO-1 is crucial for Trp metabolism into Kyn[43], we thus evaluated NJ-mediated IDO-1 inactivation by monitoring the change of Kyn to Trp ratio in the cell lysates (Fig. 6C and Supporting Information Fig. S27). In comparison with PBS group, IFN-γ significantly increased the Kyn to Trp ratio in the 4T1 tumor cells due to IFN-γ-inducible IDO-1 upregulation (Fig. 6C). The Kyn to Trp ratio was remarkably reduced by treatment with free NLG919 or NJ NPs, implying that NJ NPs inhibited the Trp metabolism activity of IDO-1. Noticeably, NJ NPs much more efficiently inhibited Trp metabolism into Kyn than free NLG919 (Fig. 6C). Along with NJ-mediated PD-L1 downregulation and IDO-1 inhibition in 4T1 breast tumor cells, the same phenomenon was observed in CT26 colorectal tumor cells (Fig. 6D–F). All above PD-L1 expression and Trp metabolism data validated the advantage of the "two-in-one" bispecific NJ prodrug for simultaneously targeting two immune evasion pathways (*i.e.*, PD-L1-induced CTLs exhaustion and IDO-1-mediated Trp consumption, Fig. 6G).

3.6. *Antitumor performance and immune assay of the prodrug NPs in 4T1 tumor model*

Given the satisfying blockade of the intrinsic and adaptive immune resistance pathways by the PHPNJ NPs, we next evaluated their antitumor performance in a 4T1 tumor-bearing BLAB/c mouse model *in vivo* (Fig. 7A). For this purpose, two PHP-coated prodrug NPs containing homogenous dimers of DN or DJ were used as the controls, which were named as PHPDN and PHPDJ, respectively. Fig. 7B and C showed that PHPNJ moderately inhibited tumor growth with tumor relapsed post treatment. In contrast, in comparison with the $PHPDN^{L}$ and $PHPDJ^{L}$ groups, the combination of PHPNJ with 671 nm laser-performed PDT ($PHPNJ^{L}$) much more efficiently inhibited 4T1 tumor growth and even eradicated the tumor xenografts (Fig. 7B and C), which also remarkably prolonged the survival of the tumor-bearing mice (Fig. 7D). To investigate the anti-metastasis profile of the prodrug NPs, the lungs of the 4T1 tumor-bearing mice were collected for histopathological H&E staining at the end of the antitumor study. In consistent with the antitumor performance, $PHPNJ^{L}$ displayed the best anti-metastasis profile and longest survival rate among all the experimental groups (Fig. 7E and F).

To exploit the mechanism underlying the superior antitumor performance of the PHPNJ NPs integrating bispecific NJ prodrug, DC maturation in the tumor-draining LNs and tumor-infiltrating T lymphocytes were examined at the end of the antitumor study. Upon 671 nm laser irradiation, the $PHPDN^{L}$, $PHPDJ^{L}$ and $PHPNJ^{L}$ groups remarkably elicited DC maturation, verifying that PDT by PHP efficiently elicited immune response by inducing ICD of the tumor cells *in vivo* (Fig. 7G and Supporting Information Fig. S28A).

Flow cytometric measurement further revealed that the $PHPNJ^{L}$ significantly promoted intratumoral infiltration of the T lymphocytes ($CD3^{+}$ T cells, Fig. S28B). In particularly, treatment by $PHPNJ^{L}$ remarkably promoted intratumoral infiltration of the $CD8^{+}$ T cells compared with the PBS group (Fig. 7H and I), which was further validated by the immunofluorescence staining of the $CD8^{+}$ T cells in the tumor section (Fig. 7J).

Along with the increased tumor infiltrating of the $CD8^{+}$ T cells, the percentage of effector T lymphocytes (*i.e.*, IFN-$\gamma^{+}CD8^{+}$ T cells) significantly increased in the tumor of the $PHPNJ^{L}$ group (Fig. S28C), which was 58.0-fold higher than that of the PBS group (Fig. 7K). ELISA analysis further confirmed significant increase of IFN-γ secretion in the tumor tissue of the $PHPNJ^{L}$ group (Fig. 7L). All these data collectively validated the activation of the protective immune response with PHPNJ-mediated combinatory therapy.

Immunohistochemical (IHC) assay revealed that combinatory therapy by i.v. injection of nanoparticles and laser irradiation noticeably elicited IDO-1 expression in the tumor treated by $PHPDN^{L}$, $PHPDJ^{L}$ and $PHPNJ^{L}$ (Fig. 7M and N), suggesting photoimmunotherapy induced the occurrence of adaptive immune resistance. Noticeably, the percentage of Tregs of $PHPNJ^{L}$ group declined dramatically from 59.7% to 14.2% compared with the PBS group (Fig. 7O). Meanwhile, the $CD8^{+}$ T cells to Tregs ratio of $PHPNJ^{L}$ group increased to 6.5, which was ~23.7-fold higher than that of the PBS group (Fig. 7P).

IHC analysis further demonstrated that $PHPDN^{L}$ upregulated PD-L1 expression in the tumor sections (Fig. 7Q), and the PD-$L1^{+}$ cells ratio was 2.0-fold higher than that of the PBS group due to PDT-triggered immune response as well as the lack of JQ1 (Fig. 7R). It was worth to noting that PD-$L1^{+}$ tumor cells of the $PHPNJ^{L}$ group were 8.0-fold lower than that of $PHPDN^{L}$ group due to the abolishment of PD-L1 expression by JQ1.

3.7. *Prodrug NPs-mediated combinatory immunotherapy in the CT26 tumor model*

To demonstrate the genericity of the prodrug NPs for potentiating cancer immunotherapy, the antitumor performance of the $PHPNJ^{L}$ group was next evaluated in a mouse model of CT26 colorectal tumors by following the same procedure applied for the 4T1 tumor model (Fig. 8A). In consistent with the antitumor performance demonstrated in 4T1 tumor model, $PHPNJ^{L}$ also efficiently suppressed CT26 tumor growth (Fig. 8B and C). The survival curves correlated well with antitumor performance of $PHPDN^{L}$ and $PHPDJ^{L}$ in CT26 and 4T1 tumor models respectively, suggesting CT26 tumor was more sensitive to IDO-1-blockade therapy than 4T1 tumor (Figs. 7D and 8D). The $PHPNJ^{L}$ group displayed the smallest tumor size and lowest tumor mass among all the experimental groups when examined at the end of the antitumor study, verifying satisfying anti-tumor effect of the PHPNJ-mediated combinatory therapy (Fig. 8E and F).

Flow cytometric assay displayed that the $PHPNJ^{L}$ group were of 5.1-fold higher DC maturation ratio than that of the PBS group in the tumor-draining LNs (Fig. 8G and Supporting Information Fig. S29A). $PHPNJ^{L}$ significantly recruited the tumor-infiltrating $CD3^{+}$ T cells (Fig. S29B), increased the percentage of $CD8^{+}$ T cells ($CD3^{+}CD8^{+}$) to 58.9% (Fig. 8H), with 5.3-fold higher $CD8^{+}$ to $CD4^{+}$ T cells ratio than that of the PBS group (Fig. 8I). Furthermore, the $PHPNJ^{L}$ group showed 41.4-fold higher tumor mass-normalized tumor-infiltrating $CD8^{+}$ T cells than that of PBS group (Fig. 8J). The increased intratumoral infiltration of the $CD8^{+}$ T lymphocytes was further validated by immunofluorescence staining assay (Fig. 8K).

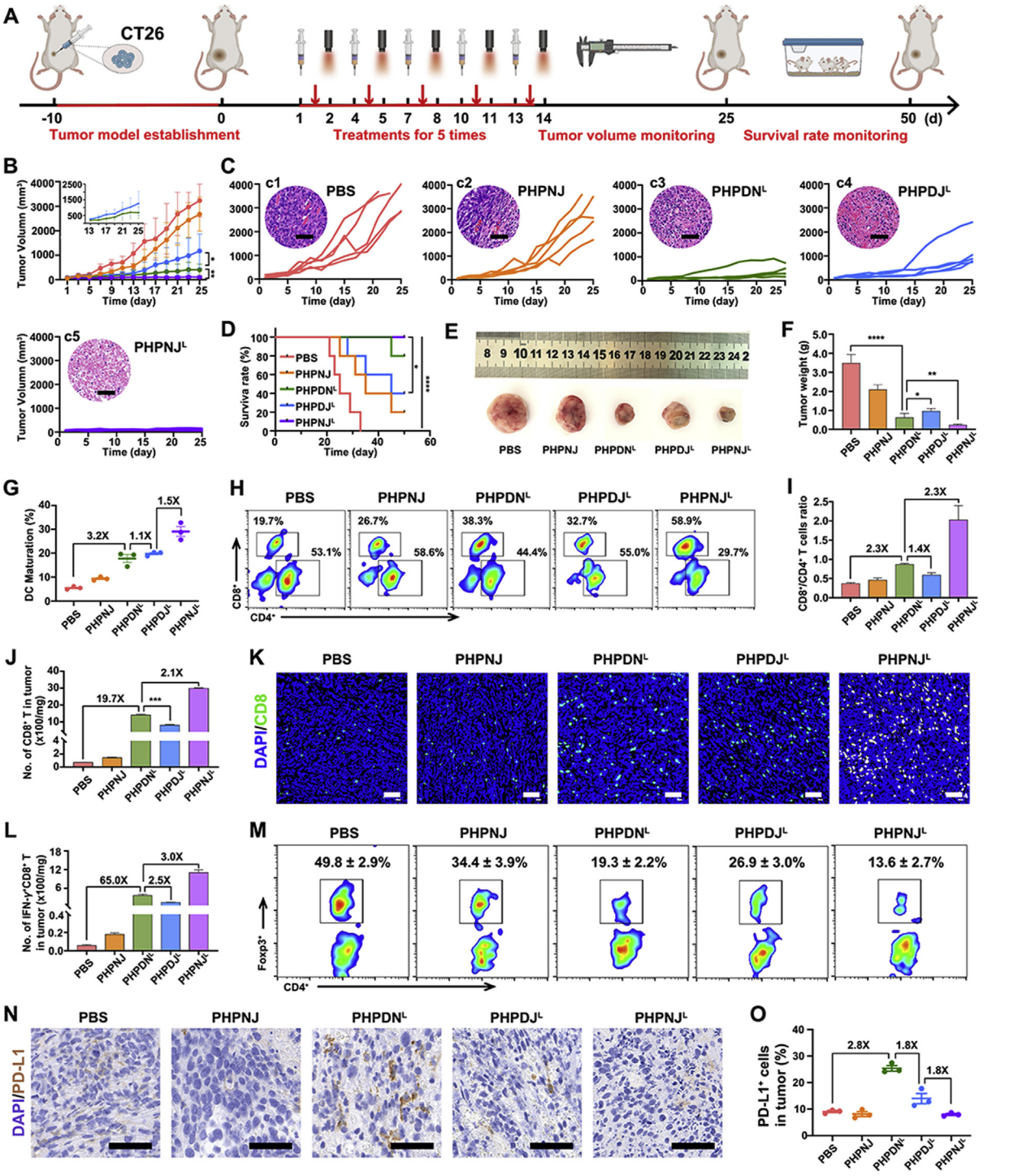

Figure 8 The antitumor efficacy and antitumor immunity of the bispecific NPs in CT26 tumor-bearing mice by circumventing the intrinsic and inducible immune resistance pathways. (A) Schematic illustration of therapeutic schedule; (B) The averaged tumor growth curves, and (C) the individual tumor growth curves of the CT26 tumor-bearing mice following different treatments ($n = 5$, the inserts showed the representative H&E images of the tumor sections, scale bar = 60 μm); (D) The survival rate of tumor-bearing mice after treatments ($n = 5$); (E) The representative photograph of the tumor tissues, and (F) the averaged tumor mass examined at the end of the antitumor study ($n = 5$); (G) DC maturation induced by various treatments ($n = 3$); (H) Flow cytometry plots of the tumor-infiltrating $CD8^+$ and $CD4^+$ T cells; (I) The ratio of the tumor-infiltrating $CD8^+$ to $CD4^+$ T cells; (J) The tumor mass-normalized number of the tumor-infiltrating $CD8^+$ T cells examined on the 5th day post-treatment; (K) The representative immunofluorescence images of the tumor-infiltrating $CD8^+$ T cells (scale bar = 50 μm); (L) The tumor mass-normalized number of the IFN-γ^+CD8^+ effector T cells examined on the 5th day post-treatment; (M) Flow cytometry plots of the tumor-infiltrating Tregs examined on the 5th day post-treatment; (N) IHC examination of PD-L1 expression in the tumor (scale bar = 50 μm), and (O) PD-L1 positive rate within tumor mass at the end of the antitumor study. The data were showed as mean ± SD. $^*P < 0.05$; $^{**}P < 0.01$; $^{***}P < 0.001$; $^{****}P < 0.0001$; n.s., not significant.

Flow cytometry examination also showed a steep increase of the tumor-infiltrating IFN-γ^+CD8$^+$ T cells in the PHPNJ^L groups (Fig. S29C). For instance, upon PHPNJ^L treatment, the percentage of IFN-γ^+CD8$^+$ T cells increased up to 37.0%, which was 4.7-fold higher than that of PBS groups (Fig. S29C). Noticeably, tumor mass-normalized tumor-infiltrating IFN-γ^+CD8$^+$ T cells in PHPDN^L group was 2.5-fold higher than that of the PHPDJ^L group, indicating the better antitumor efficacy of the PHPDN^L group in CT26 tumor (Fig. 8L).

Of note, treatment by PHPDJ^L decreased the fraction of the tumor-infiltrating Tregs (CD3$^+$CD4$^+$Foxp3$^+$) from 49.8% (PBS group) to 26.9%. In contrast, PHPDN^L and PHPNJ^L reduced the frequency of Tregs to 19.3% and 13.6%, respectively (Fig. 8M), verifying that IDO-1-inhibition contributed more than PD-L1 suppression to downregulating Tregs and relieving the immunosuppressive TME. Interestingly, IHC examination showed more pronounced upregulation of IDO-1 expression in the CT26 tumor than 4T1 tumor (Supporting Information Fig. S30), suggesting CT26 tumor might be more susceptible for IFN-γ-inducible IDO-1 expression.

Furthermore, PD-L1 expression in the PHPNJ^L group was 3.2-fold lower than that of PHPDN^L groups, validating the advantage of NJ prodrug for targeting both IDO-1 and PD-L1-mediated immune resistance (Fig. 8N and O). The tumor-bearing mice displayed negligible body weight changes, and the major organs showed invisible histopathological damage, implying good biocompatibility of PHPNJ NPs (Supporting Information Figs. S31 and S32).

Overall, the immune assay in 4T1 and CT26 tumor models both validated that the combinatory therapy by PHPNJ and PDT elicited antitumor immune response by activating the tumor-infiltrating CTLs, depleting the immunosuppressive Tregs and downregulated PD-L1 expression in the TME. In comparison with the conventional nanomedicine reported for cancer immunotherapy so far, the bispecific NJ prodrug NPs displayed distinct advantages. First, the prodrug NPs possessed good colloid stability and long blood circulation in physiological environment and subsequent excellent tumor accumulation and penetration enhanced by the tumor-activatable PHP[44]. Second, the prodrug NPs displayed consistent pharmacokinetics and release profile of two small molecule drugs with different targets to promote synergistic immune modulation and optimize the therapeutic performance of the combinatorial immunotherapy[45]. Furthermore, the prodrug NPs were of high drug loading efficacy, minimal excipient-related immunotoxicity, robust preparation procedure for scale up and clinical translation. Taken together, the bispecific prodrug nanoplatform simultaneously enhancing immunogenicity and blocking multiple immune evasion pathways might represent a promising strategy to defeat vastly dynamic and complex immune resistance for cancer combinatorial regimens involving immunotherapy.

4. Conclusions

In summary, we herein reported a bispecific prodrug NP for circumventing multiple immune evasion pathways and improving cancer immunotherapy. The “three in one” prodrug NPs composed of the tumor acidity-activatable diblock copolymer PHP for PDT of tumor, and the bispecific prodrug NJ of JQ1 and NLG919 for suppressing IFN-γ-inducible immune evasion of the tumor cells. The prodrug PHPNJ NPs displayed increased cellular uptake at acidic condition, and tumor-specific distribution and deep penetration *via* acid-triggered deshielding of the polymer shell. The prodrug NPs elicited antitumor immune response *via* PDT-induced ICD of the tumor cells, and circumvented adaptive immune resistance by inhibiting IFN-γ-inducible expression of PD-L1 and inactivating IDO-1. Combinatory immunotherapy with the prodrug NPs and PDT remarkably inhibited tumor growth and elongated animal survival in both 4T1 breast and CT26 colorectal tumor models. Immune analysis revealed that the prodrug NPs elicited robust immune response by recruiting tumor-infiltrating CTLs and depleting Tregs. This study provided a novel insight for potentiating cancer immunotherapy by addressing multiple immune evasion pathways.

Acknowledgments

This study was supported by the National Natural Science Foundation of China (51873228, 22074043), International Cooperation Project of Science and Technology Commission of Shanghai Municipality (20430711800, China), the Youth Innovation Promotion Association of CAS (2014218, China), and the Fusion Grant between Fudan University and Shanghai Institute of Materia Medica, CAS (No. FU-SIMM-20182006, China). The Mass Spectrometry System and the cell sorter BD Influx of the National Facility for Protein Science in Shanghai (NFPS), Shanghai Advanced Research Institute, CAS are gratefully acknowledged. All animal procedures were carried out under the guidelines approved by the Institutional Animal Care and Use Committee (IACUC) of the Shanghai Institute of Materia Medica, CAS.

Author contributions

Jiayi Ye, Bo Hou and Haijun Yu conceived the project and designed the study. Jiayi Ye, and Bo Hou performed the immune assay and collected the data. Jiayi Ye, and Bo Hou prepared the initial manscrupt. Jiayi Ye, Bo Hou and Haijun Yu analyzed the data. Shunan Zhang, Tianliang Li, Fangmin Chen and Zhiai Xu contributed to data analysis and manuscript revision. Muya Xiong and Yechun Xu helped to perform the molecular docking.

Conflicts of interest

The authors declare no conflict of interest.

Appendix A. Supporting information

Supporting information to this article can be found online at https://doi.org/10.1016/j.apsb.2021.09.021.

References

1. Ribas A. Adaptive immune resistance: how cancer protects from immune attack. *Cancer Discov* 2015;**5**:915−9.
2. Sharma P, Hu-Lieskovan S, Wargo JA, Ribas A. Primary, adaptive, and acquired resistance to cancer immunotherapy. *Cell* 2017;**168**:707−23.
3. Kalbasi A, Ribas A. Tumour-intrinsic resistance to immune checkpoint blockade. *Nat Rev Immunol* 2020;**20**:25−39.
4. Munn DH, Mellor AL. IDO and tolerance to tumors. *Trends Mol Med* 2004;**10**:15−8.
5. Spranger S, Spaapen RM, Zha Y, Williams J, Meng Y, Ha TT, et al. Up-regulation of PD-L1, IDO, and T(regs) in the melanoma tumor microenvironment is driven by CD8$^+$ T cells. *Sci Transl Med* 2013;**5**:200ra116.

6. Cervenka I, Agudelo LZ, Ruas JL. Kynurenines: tryptophan's metabolites in exercise, inflammation, and mental health. *Science* 2017;**357**:eaaf9794.
7. Overacre-Delgoffe AE, Chikina M, Dadey RE, Yano H, Brunazzi EA, Shayan G, et al. Interferon-γ drives T(reg) fragility to promote anti-tumor immunity. *Cell* 2017;**169**:1130−1141.e11.
8. Mellor AL, Munn DH. Tryptophan catabolism and regulation of adaptive immunity. *J Immunol* 2003;**170**:5809−13.
9. Pardoll DM. The blockade of immune checkpoints in cancer immunotherapy. *Nat Rev Cancer* 2012;**12**:252−64.
10. Restifo NP, Smyth MJ, Snyder A. Acquired resistance to immunotherapy and future challenges. *Nat Rev Cancer* 2016;**16**:121−6.
11. Hegde PS, Chen DS. Top 10 challenges in cancer immunotherapy. *Immunity* 2020;**52**:17−35.
12. O'Donnell JS, Teng MWL, Smyth MJ. Cancer immunoediting and resistance to T cell-based immunotherapy. *Nat Rev Clin Oncol* 2019;**16**:151−67.
13. Riethmüller G. Symmetry breaking: bispecific antibodies, the beginnings, and 50 years on. *Cancer Immun* 2012;**12**:12.
14. Sheridan C. Bispecific antibodies poised to deliver wave of cancer therapies. *Nat Biotechnol* 2021;**39**:251−4.
15. Chan AC, Carter PJ. Therapeutic antibodies for autoimmunity and inflammation. *Nat Rev Immunol* 2010;**10**:301−16.
16. Labrijn AF, Janmaat ML, Reichert JM, Parren P. Bispecific antibodies: a mechanistic review of the pipeline. *Nat Rev Drug Discov* 2019;**18**:585−608.
17. Weidanz J. Targeting cancer with bispecific antibodies. *Science* 2021;**371**:996−7.
18. Saeed M, Chen F, Ye J, Shi Y, Lammers T, De Geest BG, et al. From design to clinic: engineered nanobiomaterials for immune normalization therapy of cancer. *Adv Mater* 2021;**33**:2008094.
19. Chan WCW. Nanomedicine 2.0. *Acc Chem Res* 2017;**50**:627−32.
20. Shi J, Kantoff PW, Wooster R, Farokhzad OC. Cancer nanomedicine: progress, challenges and opportunities. *Nat Rev Cancer* 2017;**17**:20−37.
21. Xu X, Ho W, Zhang X, Bertrand N, Farokhzad O. Cancer nanomedicine: from targeted delivery to combination therapy. *Trends Mol Med* 2015;**21**:223−32.
22. Yang B, Gao J, Pei Q, Xu H, Yu H. Engineering prodrug nanomedicine for cancer immunotherapy. *Adv Sci* 2020;**7**:2002365.
23. Wang Y, Wang J, Zhu D, Wang Y, Qing G, Zhang Y, et al. Effect of physicochemical properties on *in vivo* fate of nanoparticle-based cancer immunotherapies. *Acta Pharm Sin B* 2021;**11**:886−902.
24. Peng J, Xiao Y, Li W, Yang Q, Tan L, Jia Y, et al. Photosensitizer micelles together with IDO inhibitor enhance cancer photothermal therapy and immunotherapy. *Adv Sci* 2018;**5**:1700891−1115.
25. Yang Q, Shi G, Chen X, Lin Y, Cheng L, Jiang Q, et al. Nanomicelle protects the immune activation effects of paclitaxel and sensitizes tumors to anti-PD-1 immunotherapy. *Theranostics* 2020;**10**:8382−99.
26. Li M, Zhao L, Zhang T, Shu Y, He Z, Ma Y, et al. Redox-sensitive prodrug nanoassemblies based on linoleic acid-modified docetaxel to resist breast cancers. *Acta Pharm Sin B* 2019;**9**:421−32.
27. Yu J, Wang Y, Zhou S, Li J, Wang J, Chi D, et al. Remote loading paclitaxel−doxorubicin prodrug into liposomes for cancer combination therapy. *Acta Pharm Sin B* 2020;**10**:1730−40.
28. Zhou S, Li J, Yu J, Yang L, Kuang X, Wang Z, et al. A facile and universal method to achieve liposomal remote loading of non-ionizable drugs with outstanding safety profiles and therapeutic effect. *Acta Pharm Sin B* 2021;**11**:258−70.
29. Castano AP, Mroz P, Hamblin MR. Photodynamic therapy and anti-tumour immunity. *Nat Rev Cancer* 2006;**6**:535−45.
30. Aune TM, Pogue SL. Inhibition of tumor cell growth by interferon-gamma is mediated by two distinct mechanisms dependent upon oxygen tension: induction of tryptophan degradation and depletion of intracellular nicotinamide adenine dinucleotide. *J Clin Invest* 1989;**84**:863−75.
31. Sheridan C. IDO inhibitors move center stage in immuno-oncology. *Nat Biotechnol* 2015;**33**:321−2.
32. Filippakopoulos P, Knapp S. Targeting bromodomains: epigenetic readers of lysine acetylation. *Nat Rev Drug Discov* 2014;**13**:337−56.
33. Zhu H, Bengsch F, Svoronos N, Rutkowski MR, Bitler BG, Allegrezza MJ, et al. BET bromodomain inhibition promotes anti-tumor immunity by suppressing PD-L1 expression. *Cell Rep* 2016;**16**:2829−37.
34. Hou B, Zhou L, Wang H, Saeed M, Wang D, Xu Z, et al. Engineering stimuli-activatable boolean logic prodrug nanoparticles for combination cancer immunotherapy. *Adv Mater* 2020;**32**:1907210−1.
35. Wang T, Wang D, Liu J, Feng B, Zhou F, Zhang H, et al. Acidity-triggered ligand-presenting nanoparticles to overcome sequential drug delivery barriers to tumors. *Nano Lett* 2017;**17**:5429−36.
36. Ma Y, Mou Q, Zhu X, Yan D. Small molecule nanodrugs for cancer therapy. *Mater Today Chem* 2017;**4**:26−39.
37. Wang Y, Liu D, Zheng Q, Zhao Q, Zhang H, Ma Y, et al. Disulfide bond bridge insertion turns hydrophobic anticancer prodrugs into self-assembled nanomedicines. *Nano Lett* 2014;**14**:5577−83.
38. Sun Q, Radosz M, Shen Y. Challenges in design of translational nanocarriers. *J Control Release* 2012;**164**:156−69.
39. Zhu Q, Saeed M, Song R, Sun T, Jiang C, Yu H. Dynamic covalent chemistry-regulated stimuli-activatable drug delivery systems for improved cancer therapy. *Chin Chem Lett* 2020;**31**:1051−9.
40. Gao J, Wang WQ, Yu HJ. Acid-activatable polymeric drug delivery systems for cancer therapy. *Acta Polym Sin* 2010;**41**:986−94.
41. Gao A, Chen B, Gao J, Zhou F, Saeed M, Hou B, et al. Sheddable prodrug vesicles combating adaptive immune resistance for improved photodynamic immunotherapy of cancer. *Nano Lett* 2020;**20**:353−62.
42. Obeid M, Tesniere A, Ghiringhelli F, Fimia GM, Apetoh L, Perfettini JL, et al. Calreticulin exposure dictates the immunogenicity of cancer cell death. *Nat Med* 2007;**13**:54−61.
43. Du L, Xing Z, Tao B, Li T, Yang D, Li W, et al. Both IDO1 and TDO contribute to the malignancy of gliomas *via* the Kyn-AhR-AQP4 signaling pathway. *Signal Transduct Target Ther* 2020;**5**:10.
44. Zhang M, Gao S, Yang D, Fang Y, Lin X, Jin X, et al. Influencing factors and strategies of enhancing nanoparticles into tumors *in vivo*. *Acta Pharm Sin B* 2021;**11**:2265−85.
45. Cheng X, Li D, Xu J, Wei B, Fang Q, Yang L, et al. Self-assembled ternary hybrid nanodrugs for overcoming tumor resistance and metastasis. *Acta Pharm Sin B* 2021;**11**:3595−607.